Automatic Segmentation of Intra-Treatment CT Images for Adaptive Radiation Therapy of the Prostate

B.C. Davis[1,2], M. Foskey[1,2], J. Rosenman[2], L. Goyal[2], S. Chang[2], and S. Joshi[1,2]

[1] Department of Computer Science, University of North Carolina, USA,
{davisb,joshi}@cs.unc.edu,
[2] Department of Radiation Oncology, University of North Carolina, USA.

Abstract. We have been developing an approach for automatically quantifying organ motion for adaptive radiation therapy of the prostate. Our approach is based on deformable image registration, which makes it possible to establish a correspondence between points in images taken on different days. This correspondence can be used to study organ motion and to accumulate inter-fraction dose. In prostate images, however, the presence of bowel gas can cause significant correspondence errors. To account for this problem, we have developed a novel method that combines large deformation image registration with a bowel gas segmentation and deflation algorithm. In this paper, we describe our approach and present a study of its accuracy for adaptive radiation therapy of the prostate. All experiments are carried out on 3-dimensional CT images.

1 Introduction

One major treatment method for prostate cancer is external beam radiation therapy, which uses high energy x-rays that are delivered in a series of 40 or more daily treatments. To be safe and effective, the radiation dose to the cancer-containing prostate should be as high as possible while the dose to surrounding organs such as the rectum and bladder must be limited. This effect is achieved by using multiple radiation beams that overlap on the tumor and are shaped to exclude normal tissue as much as possible. However, internal organ motion and patient setup errors present a serious challenge to this approach. The prostate, rectum, bladder and other organs move in essentially unpredictable ways, and even small changes in their position can result in either tumor under-dosing, normal tissue over-dosing, or both.

Adaptive radiation therapy (ART), which uses periodic intra-treatment CT images for localization of the tumor and radiosensitive normal structures, is being investigated to meet this challenge. In this method a feedback control strategy [1] is used to correct for differences in the planned and delivered dose distributions due to spatial changes in the treatment volume early in the treatment period.

Although in-treatment-room CT scanners provide the enabling imaging hardware to implement ART, no software methods or tools for automatic image processing exist to enable the incorporation of these images in the adaptive

treatment of prostate or other cancer. As a result, all such work must be done manually. However, manual segmentation of the tumor and neighboring organs places an impractical burden on highly skilled and already overburdened personnel. Moreover, clinically significant inter- and intra-user variability of manual segmentations introduces a source of treatment uncertainty that current adaptive radiation therapy techniques do not address [2, 3].

We have been developing an approach for automatically quantifying organ motion over the course of treatment. Our approach is based on deformable image registration, which makes it possible to establish a correspondence between points in images taken on different days. This correspondence can be used to study organ motion and to accumulate inter-fraction dose.

In prostate images, however, the presence of bowel gas can cause significant correspondence errors as no correspondence exists for pockets of gas across different days. Shown in Figure 1 are two rigidly aligned axial images of a patient taken on two different days. Due to the transient nature of bowel gas, it is present in one of the days but absent in the other. To account for this problem, we have developed a novel method that combines large deformation image registration with a bowel gas segmentation and deflation algorithm. In this paper, we describe our approach and present a study of its accuracy for adaptive radiation therapy of the prostate.
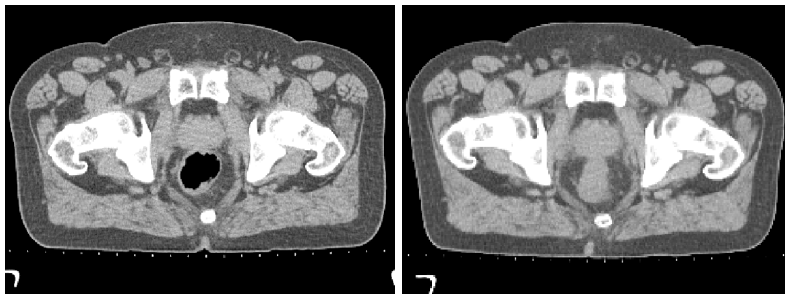

Fig. 1. Axial CT slice of the same patient acquired on different days, showing the effect of bowel gas.

Several deformable image registration methods are currently being investigated for alignment of serial CT data [4–7]. However, none of these studies address the problem of bowel gas for deformable registration of CT images. Also, while some authors present validation studies based on known transformations or phantoms, to our knowledge none have presented an analysis of the accuracy of their methods for automatic segmentation of a large number of treatment images based on physician drawn contours.

2   Methods

We use the CT taken at planning time, the *planning image*, as a reference. On each treatment day, the patient is positioned and then, prior to treatment, a new CT scan is acquired using an in-treatment-room CT scanner that shares a table with the linear accelerator. Each *treatment image* characterizes the patient configuration at that treatment time.

If there were absolutely no organ motion then the planning and treatment images should all be the same, except for noise from the imaging device. However, because there is organ motion, these images will differ, and the difference characterizes the organ motion. We have understood the motion when we can tell, for each point in the planning image, which point in the treatment image it corresponds to. In this way organ motion and image registration are linked—we can understand organ motion if we can estimate image correspondence.

We can view an image as a function I from the spatial domain $\Omega \subset \mathbb{R}^3$ to an intensity value in $\mathbb{R}$. Image correspondence is expressed as a function $h \colon \Omega \to \Omega$, called a *deformation field*. For $x \in \Omega$, $h(x)$ is the point in the treatment image, I_T, that corresponds to the point x in the planning image, I_P.

The transformation h is estimated as follows. First, the planning and treatment CT data sets are rigidly registered. This quantifies the rigid patient setup error. In order to accommodate bowel gas we apply our algorithm for segmenting and deflating bowel gas to produce deflated images I_{P_d} and I_{T_d}. Finally, I_{P_d} and I_{T_d} are registered using a high dimensional large-deformation image registration algorithm. h is defined as the composition of these transformations.

Rigid Registration The planning and treatment images are thresholded so that only bone is visible. The region of interest is restricted to the pelvis as it remains fixed while the femurs and spine can rotate or bend. The rigid transformation, r, is estimated using an intensity based gradient descent algorithm [8].

Accommodating Bowel Gas As the contrast between gas and surrounding tissue is very high in CT images, we create a binary segmentation of the gas in an image using a simple thresholding operation. We refine this binary segmentation using a morphological close operation, which eliminates small pockets of gas. Next, we construct a deflation transformation s based on a flow induced by the gradient of the binary image. Points along the gas-tissue border, where the gradient is non-zero, flow in the direction of the gradient. As a result, gas filled regions collapse toward their medial skeletons—deflating like a balloon. Importantly, we do not aim to simulate the true motion of the tissue but to deflate the gas so that the image may be accurately registered.

More precisely, we construct a non-diffeomorphic deflation transformation $s \colon \Omega \to \Omega$ such that $I(s(x))$ is the image $I(x)$ after a deformation that deflates gas. The transformation s is constructed by integrating velocity fields $v(x,t)$ forward in time, i.e. $s(x) = x + \int_0^1 v(s(x,t),t)\,dt$. These velocity fields are induced by a force function $F(x,t) = \nabla(I \circ s_t)(x)$ that is the gradient of the binary image. The force function and velocity fields are related by the modified Navier-Stokes operator $(\alpha \nabla^2 + \beta \nabla (\nabla \cdot) + \gamma)v(x,t) = F(x,t)$. We solve for s using an iterative greedy method.

Figure 2 shows the result of our gas deflation algorithm. The large pocket of gas present in the image has been deflated, resulting in an image that can be accurately registered using deformable image registration.

Deformable Image Registration We apply the theory of large deformation diffeomorphisms [9, 10] to generate a deformation $h_{\text{def}} \colon \Omega_{P_d} \to \Omega_{T_d}$ that defines a voxel-to-voxel correspondence between the two gas deflated images I_{P_d}
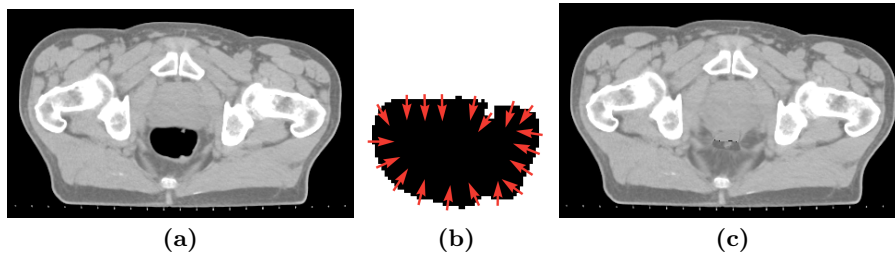
Fig. 2. Gas Deflation Algorithm. (a) Axial slice CT image with large pocket of bowel gas. (b) Zoomed in on the gas pocket. The gas is segmented using simple thresholding. Gas is deflated by a flow induced by the gradient of the binary image. (c) The image after application of the deflation transformation.

and I_{T_d}. The registration is determined by finding the deformation field h_{def} that minimizes the mean squared error between I_{P_d} and the deformed image $I_{T_d} \circ h_{\text{def}}$,

$$D(h) = \int_{x \in \Omega} |I_{P_d}(x) - I_{T_d}(h_{\text{def}}(x))|^2 \, dx.$$

The transformation is constrained to be diffeomorphic by enforcing that it satisfy laws of continuum mechanics derived from visco-elastic fluid modeling [10, 9].

Composite Transformation Correspondence between the original images I_P and I_T is estimated by concatenating the rigid, deflation, and deformable registration transformations, i.e.

$$h_{P \to T} = r(s_T(h_{\text{def}}(s_P^{-1}(x))))).$$

That is, the point x in the planning image corresponds to the point $h_{P \to T}(x)$ in the treatment image. This composite transformation is not guaranteed to be diffeomorphic. However, the non-diffeomorphic part of the transformation is restricted to the region of the rectum that contains gas—where no correspondence exists.

Figure 3 shows an example of the application of method described above. Panel (b) shows the result of automatic segmentation using only large deformation image registration. Manually drawn contours of the prostate and rectum are mapped, using this correspondence, from the reference image (a) onto the daily image. Manual contours are drawn in red while mapped contours are drawn in yellow. Notice the misalignment of the manual and automatically generated contours in the daily image; the presence of bowel gas has caused correspondence errors around the rectum. A more accurate correspondence between the reference and daily images is established by concatenating registration and deflation transformations as shown in panel (c). Notice the close alignment between the manual contours and the contours generated by our method.

3 Results

We now present detailed statistical analysis of the application of our methods to a set of 40 CT images from 3 patients undergoing ART in our clinic. Each
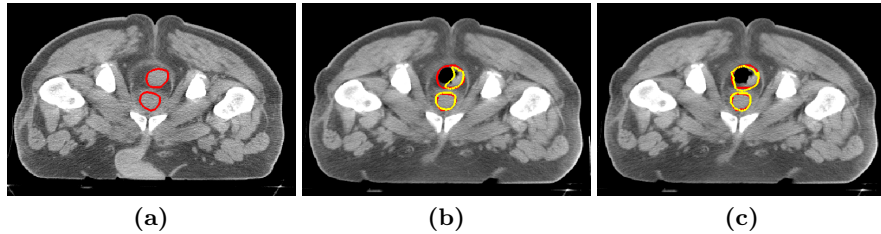
Fig. 3. Automatic segmentation of the prostate and rectum. Manually segmented structures in the planning image (a) are mapped to the daily image (b) *before* accounting for bowel gas, and (c) *after* accounting for bowel gas with our gas deflation algorithm. Manually drawn contours are shown in red and mapped contours are shown in yellow.

CT scan was collected on a Siemens Primatom CT-on-rails scanner with resolution $0.098 \times 0.098 \times 0.3$ cm. We analyze the accuracy of our method by comparing automatically generated segmentations to manual, hand-drawn, segmentations. Because of inter-rater variability, however, there is no ground truth manual segmentation to compare against. We therefore compare our automatically generated segmentations with the segmentations from two different manual raters, and then make the same comparisons between the segmentations from the manual raters.

The experimental setup is as follows. The planning image for each patient is manually segmented by rater A. Each treatment image is manually segmented twice, once by rater A and once by rater B. For each patient, our method is used to compute the transformations h_i that map the planning image onto the treatment image for each day of treatment i. An automatic segmentation is generated for each treatment image by applying h_i to the segmentation in the planning image. We can consider our automatic method for producing treatment image segmentations as rater C (for "computer").

Each segmentation is represented by a triangulated surface. For manual segmentations, the surface is constructed by applying the power crust algorithm [11] to a set of contours drawn in the axial plane by the manual raters. For automatic segmentations, the surface is generated by applying a transformation h to the vertices of the surface given by the manual segmentation in the planning image.

For each patient and for each treatment day, we make three comparisons: **CA**, automatic segmentation verses manual segmentation by rater A; **CB**, automatic segmentation verses manual segmentation by rater B; and **BA**, manual segmentation by rater B verses manual segmentation by rater A. It should be emphasized that the automatic segmentations are produced by transforming manual planning segmentations produced by rater A, not rater B. Thus, we expect the CA comparisons to be more favorable than the CB comparisons.

In the rest of this section, we present the results of this experiment when comparing centroid differences and relative volume overlap of segmentations.

Centroid Analysis The centroid of the prostate is especially important for radiation treatment planning and therapy because it is the origin, or isocen-

ter, for the treatment plan. To measure the accuracy of our automatic segmentations with respect to centroid measurement, we compare the centroid of each automatic segmentation with the centroids of the corresponding manual segmentations. The differences in the lateral (X), anterior-posterior (Y), and superior-inferior (Z) directions are measured separately.

Figure 4 shows box and whisker plots of these differences for CA, CB, and BA comparisons. All measurements are made in centimeters. Additional summary statistics are presented in table 1.
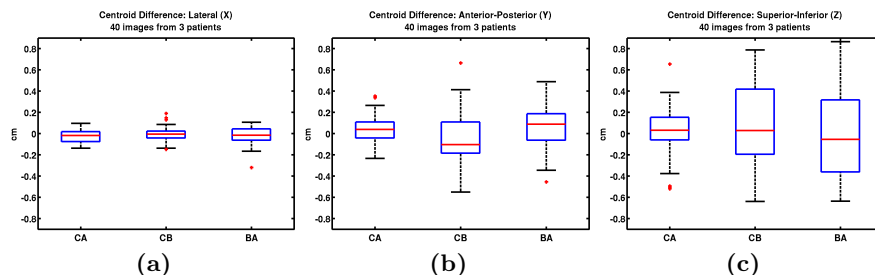

(a) (b) (c)

Fig. 4. Centroid differences in the lateral (X), anterior-posterior (Y), and superior-inferior (Z) directions (cm). The horizontal lines on the box plots represent the lower quartile, median, and upper quartile values. The whiskers show the extent of the rest of the data. Outliers, which fall outside 1.5 times the interquartile range, are denoted with the '+' symbol.

Centroid Difference Summary (cm)									
	Lateral (X)			A-P (Y)			Sup-Inf (Z)		
	CA	CB	BA	CA	CB	BA	CA	CB	BA
mean	-0.026	-0.007	-0.022	0.035	-0.052	0.070	0.022	0.065	-0.046
median	-0.018	-0.004	-0.015	0.040	-0.104	0.089	0.030	0.028	-0.054
std. dev.	0.06	0.07	0.08	0.14	0.23	0.20	0.24	0.38	0.38
99% CI min	-0.047	-0.030	-0.049	-0.010	-0.129	0.007	-0.054	-0.058	-0.167
99% CI max	-0.006	0.016	0.004	0.081	0.023	0.133	0.10	0.189	0.073

Table 1. Summary statistics showing mean, median, standard deviation, and 99% confidence interval of the mean for centroid differences.

Shown in Table 1 are the 99% confidence intervals for the true mean of each distribution of centroid differences. The confidence intervals for the means of the CA and CB differences both overlap with the confidence interval of the differences between human raters (AB), and are on the order of one voxel. Note that the superior-inferior (Z) direction has a slice thickness of 0.3 cm. We conclude that the automatic segmentation method is as accurate for estimating centroids as human raters and, as seen by the standard deviations, just as reliable.

Relative Volume Overlap Analysis A measure often reported for comparison of segmentations is relative volume overlap. This measure has been defined in several ways. For this study, we use the Dice Similarity Coefficient (DSC) [12] which is defined for two segmentations S_1 and S_2 as

$$\text{DSC}(S_1, S_2) = \frac{\text{Volume}(S_1 \cap S_2)}{\left(\frac{\text{Volume}(S_1 \cup S_2) + \text{Volume}(S_1 \cap S_2)}{2}\right)}. \tag{1}$$

Figure 5 (a) shows a box and whisker plot of the relative volume overlap for the CA, CB, and BA comparisons. To statistically quantify the difference between the relative volume overlaps of the three segmentations A, B, and C, we performed right sided t-tests with the alternative hypothesis $X > Y$. Figure 5, panel (c), reports the P-values of these tests. It can be seen from the table that the volume overlap measures for the CA comparisons are significantly higher than the volume overlap measure for the manual rater comparison BA. There is also no statistically significant difference between the relative volume overlaps from the CB comparison with the two manual raters. Also note that the automatic segmentations have a significantly better overlap with rater A than with rater B. This is expected as the planning image was segmented by rater A.
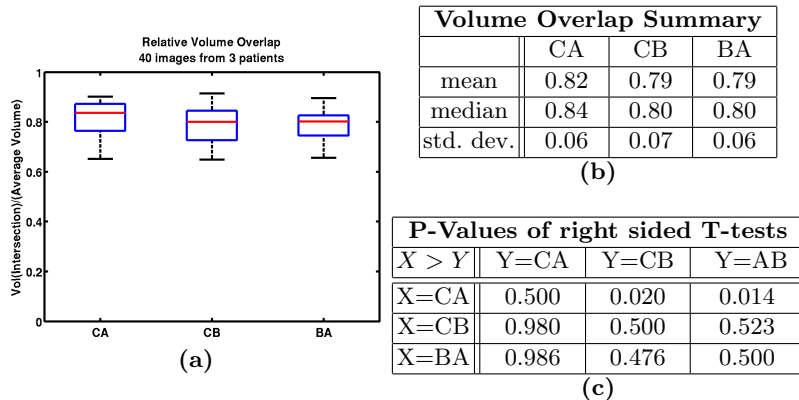

Volume Overlap Summary

	CA	CB	BA
mean	0.82	0.79	0.79
median	0.84	0.80	0.80
std. dev.	0.06	0.07	0.06

(b)

P-Values of right sided T-tests

$X > Y$	Y=CA	Y=CB	Y=AB
X=CA	0.500	0.020	0.014
X=CB	0.980	0.500	0.523
X=BA	0.986	0.476	0.500

(c)

(a)

Fig. 5. **(a)** Relative volume overlap as measured by Equation 1. **(b)** Volume overlap summary statistics. **(c)** P-value results of right sided t-test comparing the relative volume overlaps between the various raters.

4   Conclusion

We have presented an approach for automatically quantifying organ motion for adaptive radiation therapy of the prostate. This method extends deformable image registration to accommodate bowel gas, which creates image regions where no correspondence exists. We statistically analyzed the accuracy of our automatic method against the standard of manual inter-rater variation. We showed that for centroid and volume overlap of the prostate, the automatic method is statistically indistinguishable from human raters. We are currently working on applying our

method to a larger number of patients and evaluating the clinical effect of organ motion by measuring effective delivered dose and biological effect.

5 Acknowledgments

References

1. Yan, D., Lockman, D., Brabbins, D., Tyburski, L., Martinez, A.: An off-line strategy for constructing a patient-specific planning target volume in adaptive treatment process for prostate cancer. International Journal of Radiation Oncology*Biology*Physics **48** (2000) 289–302
2. van Herk, M., Bruce, A., Guus Kroes, A.P., Shouman, T., Touw, A., Lebesque, J.V.: Quantification of organ motion during conformal radiotherapy of the prostate by three dimensional image registration. International Journal of Radiation Oncology*Biology*Physics **33** (1995) 1311–1320
3. Ketting, C.H., Austin-Seymour, M., Kalet, I., Unger, J., Hummel, S., Jacky, J.: Consistency of three-dimensional planning target volumes across physicians and institutions. International Journal of Radiation Oncology*Biology*Physics **37** (1997) 445–453
4. Christensen, G.E., Carlson, B., Chao, K.S.C., Yin, P., Grigsby, P.W., N, K., Dempsey, J.F., Lerma, F.A., Bae, K.T., Vannier, M.W., Williamson, J.F.: Image-based dose planning of intracavitary brachytherapy: registration of serial-imaging studies using deformable anatomic templates. International Journal of Radiation Oncology*Biology*Physics **51** (2001) 227–243
5. Schaly, B., Kempe, J.A., Bauman, G.S., Battista, J.J., Dyk, J.V.: Tracking the dose distribution in radiation therapy by accounting for variable anatomy. Physics in Medicine and Biology **49** (2004) 791–805
6. Lu, W., Chen, M., Olivera, G.H., Ruchala, K.J., Mackie, T.R.: Fast free-form deformable registration via calculus of variations. Physics in Medicine and Biology **49** (2004) 3067–3087
7. Wang, H., Dong, L., O'Daniel, J., Mohan, R., Garden, A.S., Ang, K.K., Kuban, D.A., Bonnen, M., Chang, J.Y., Cheung, R.: Validation of an accelerated 'demons' algorithm for deformable image registration in radiation therapy. Physics in Medicine and Biology **50** (2005) 2887–2905
8. Joshi, S., Lorenzen, P., Gerig, G., Bullitt, E.: Structural and radiometric asymmetry in brain images. Medical Image Analysis **7** (2003) 155–170
9. Miller, M.I., Joshi, S.C., Christensen, G.E.: Large deformation fluid diffeomorphisms for landmark and image matching. In Toga, A.W., ed.: Brain Warping. Academic Press (1999)
10. Christensen, G.E., Rabbitt, R.D., Miller, M.I.: Deformable templates using large deformation kinematics. IEEE Transactions On Image Processing **5** (1996) 1435–1447
11. Amenta, N., Choi, S., Kolluri, R.K.: The power crust. In: ACM Symposium on Solid Modeling and Applications. (2001) 249–260
12. Dice, L.R.: Measures of the amount of ecologic association between species. Ecology **26** (1945) 297–302